

Broad-Band External Modulation Fiber-Optic Links for Antenna-Remoting Applications

Edward I. Ackerman, *Member, IEEE*, and Afshin S. Daryoush, *Senior Member, IEEE*

Abstract—We present a 6–12-GHz external modulation fiber-optic link with a spurious-free dynamic range (SFDR) of $65.5 \text{ dB} \cdot \text{MHz}^{2/3}$. This result validates an analytical model for external modulation link performance which we have updated from a previously published model to account for the use of a traveling-wave external modulator. Using the revised model, we compare the expected performance of two different link architectures.

Index Terms—Modeling, noise, nonlinearities, optical fiber communication, optical modulation/demodulation, optoelectronic devices.

I. INTRODUCTION

THE near-zero dispersion and attenuation characteristics of optical fiber render it an attractive medium for microwave and millimeter-wave antenna remoting. However, to meet the dynamic range (DR) requirements of SATCOM antenna systems, the design of a millimeter-wave fiber-optic remoting link must begin with proper choice and optimization of the electro-optic transducers. The ability to accurately model an analog fiber-optic link's broad-band performance leads to prudent device selection and optimization.

Currently, external modulation links can outperform direct modulation links across broad microwave and millimeter-wave frequency bands, because the lasers having the lowest noise optical output are ones that cannot be directly modulated at these frequencies. Several investigators have presented models for links using Mach-Zehnder interferometric external modulators [1]–[5]. In this paper, we update a model [6] which combines the most useful features of these, allowing prediction of broad-band external modulation link performance for a broad range of conditions, including: 1) traveling-wave modulator electrodes with any characteristic impedance, any complex propagation constant, and any termination impedance; 2) any passive impedance matching technique; 3) any modulator bias voltage, and; 4) any microwave or millimeter-wave frequency (inside or outside the bandwidth set by impedance matching) where device parameters are known. We present the measured performance of a 6–12-GHz external modulation link, which

Manuscript received December 3, 1996; revised April 28, 1997. This work was supported in part by NASA, Lewis Research Center, and in part by U.S. Army CECOM.

E. I. Ackerman was with the Microwave Photonics Device Laboratory, ECE Department, Drexel University, Philadelphia, PA 19104 USA. He is now with MIT Lincoln Laboratory, Lexington, MA 01273 USA.

A. S. Daryoush was with NTT Wireless Systems Laboratories, NTT Opto-Electronics Laboratories, Atsugi-shi, Yokosuka-shi, Kanagawa, Japan. He is now with the ECE Department, Drexel University, Philadelphia, PA 19104 USA.

Publisher Item Identifier S 0018-9480(97)06006-7.

agrees well with the performance predicted by the model, attesting to its usefulness.

Lastly, we describe a link architecture which differs from the one most often proposed for antenna-remoting systems. We use our modeling capability to show that this alternative link architecture can lead to improved performance at microwave and millimeter-wave frequencies.

II. EXTERNAL MODULATION LINK PERFORMANCE MODEL

At the input to an analog fiber-optic link, a microwave or millimeter-wave signal modulates the optical carrier which is to propagate in an optical fiber. The carrier is preferably a wavelength such as 1.3 or 1.55 μm , at which commercially available optical fiber has low attenuation and dispersion. At the other end of the fiber, the modulating signal is retrieved from the optical carrier and electronically coupled to the output of the link.

In [6], we have derived a model for the analog performance of an external modulation link. That model was valid only for frequencies at which the electrodes of the modulator could be modeled as lumped elements—that is, for frequencies at which the electrical wavelength was much greater than the electrode length. We later expanded this model [7] to account for the effects of nonquarter-wave bias operation. In the analysis that follows, we further generalize the model to account for use of a modulator with traveling-wave electrodes [cf. Fig. 1(a) and (b)], which is necessary for external modulation of an optical carrier at millimeter-wave frequencies.

A. Traveling-Wave Modulator

The electrodes of a traveling-wave modulator (in which electrode length is a significant fraction of, or greater than, the RF modulation wavelength) can be modeled as a transmission line of characteristic impedance Z_C terminated by a load impedance Z_t . Fig. 1(b) shows a distributed circuit model for a generalized coplanar electrode structure consisting of N periodic phase-reversed sections. The electrode phase-reversing technique helps to overcome a modulation bandwidth limitation imposed by a mismatch between the electrical and optical-wave velocities [8]. For a traveling-wave modulator without phase-reversal electrodes, N is equal to 1. The impedance $Z_M(z)$ looking toward the load Z_t from a position z along the electrodes is [9]

$$Z_M(z) = Z_C \frac{Z_t + Z_C \tanh \gamma_e z}{Z_C + Z_t \tanh \gamma_e z} \quad (1)$$

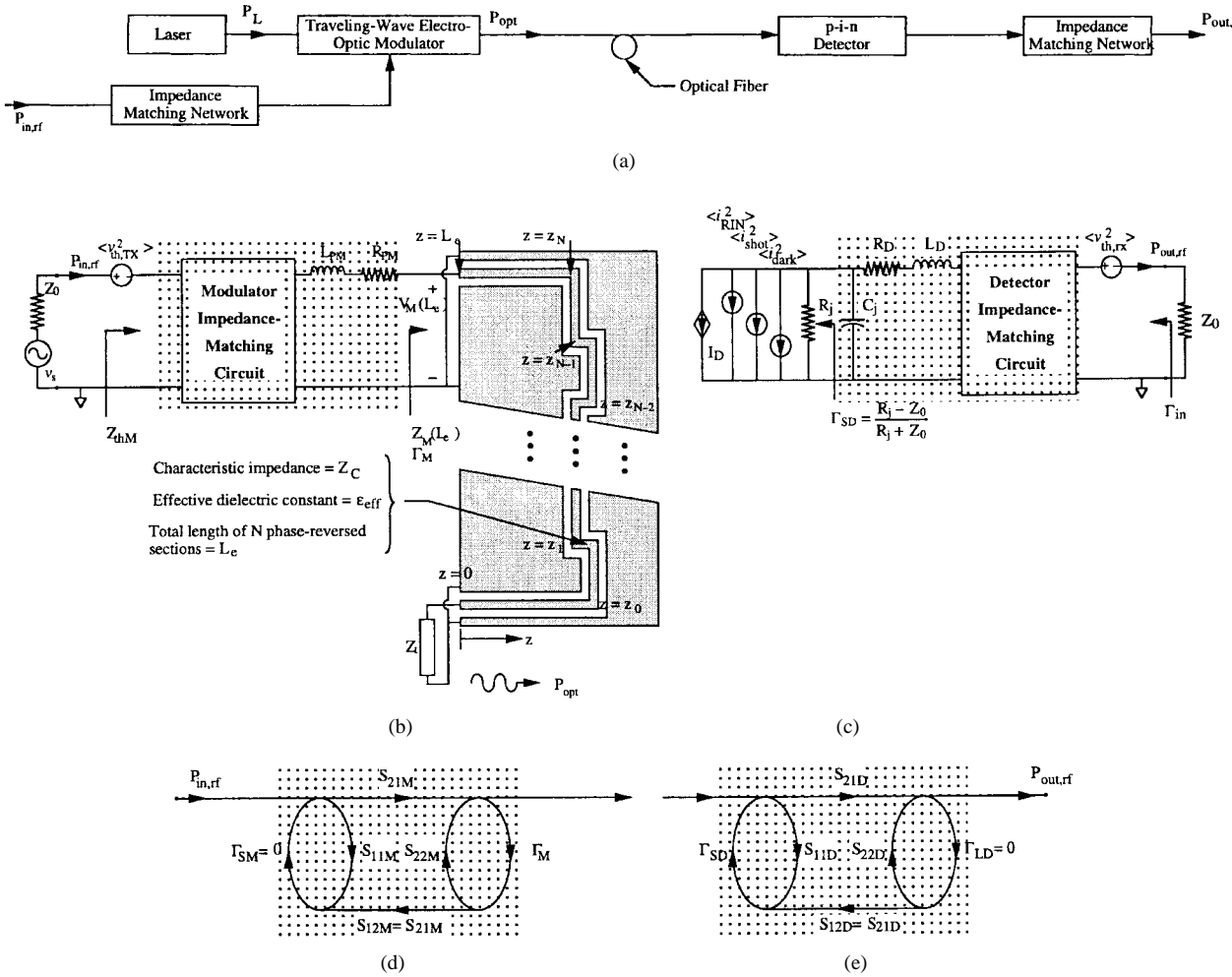


Fig. 1. Analytical model of external modulation link. (a) Schematic diagram. (b) Equivalent circuit of impedance-matched modulator in the optical transmitter. (c) Equivalent circuit of impedance-matched detector in the optical receiver. (d) SFD for optical transmitter. (e) SFD for optical receiver.

where the electrical propagation constant γ_e has real and imaginary parts α_e and $j\beta_e$. Most external modulator models assume electrodes with negligible loss (i.e., $|\alpha_e| \ll |\beta_e|$) and a characteristic impedance equal to the termination impedance. In general, these are seldom accurate assumptions for traveling-wave modulators operating across broad ranges of microwave and millimeter-wave frequencies. Modeling the traveling-wave modulator thus requires that Z_C , Z_t , α_e , and β_e be determined from its equivalent circuit, which is obtained by selecting logical element values for the model so that its impedance yields the reflection coefficient of

$$\Gamma_M = \frac{Z_M(L_e) - Z_0}{Z_M(L_e) + Z_0}. \quad (2)$$

This reflection coefficient is de-embedded from a measurement of the scattering parameter at the packaged modulator's RF input port. In (2), L_e is the total length of the modulator transmission line. Note that Z_M at any frequency is unaffected by the phase-reversal process (and is, therefore, independent of N). How the phase-reversed electrode structure affects the modulator transfer function is via the relationship between the optical power output and the voltage input.

In Mach-Zehnder modulators, a coherent optical wave is split into two paths; intensity modulation is achieved by phase-

modulating the optical carrier in one path relative to the other and interferometrically combining the two paths. For a traveling-wave Mach-Zehnder modulator, the unmodulated CW optical output power and the magnitudes of modulated output power at fundamental frequency ω_1 and third-order intermod frequency $2\omega_2 - \omega_1$ are, respectively,

$$\begin{aligned} P_{\text{opt}}(\text{DC}) &= L_M P_L \cos^2 \left(\frac{\pi V_b}{2V_g} - \frac{\pi}{4} \right) \\ &= \frac{L_M P_L}{2} \left[1 + \sin \left(\frac{\pi V_b}{V_g} \right) \right] \end{aligned} \quad (3)$$

$$\begin{aligned} P_{\text{opt}}(\omega_1) &= L_M P_L J_0 \left(\frac{2A(\omega_1)v_M}{\pi} \right) J_1 \left(\frac{2A(\omega_1)v_M}{\pi} \right) \\ &\times \cos \left(\frac{\pi V_b}{V_\pi} \right) \end{aligned} \quad (4)$$

and

$$\begin{aligned} P_{\text{opt}}(2\omega_2 - \omega_1) &= L_M P_L J_1 \left(\frac{2A(2\omega_2 - \omega_1)v_M}{\pi} \right) \\ &\times J_2 \left(\frac{2A(2\omega_2 - \omega_1)v_M}{\pi} \right) \cos \left(\frac{\pi V_b}{V_\pi} \right). \end{aligned} \quad (5)$$

In (3)–(5), P_L is the optical power coupled into the modulator, L_M is the modulator's optical insertion loss, and V_π is its

dc half-wave voltage. We define $V_b = 0$ as the quarter-wave bias voltage, and J_0 , J_1 , and J_2 denote the ordinary Bessel functions of the zeroth, first, and second order, respectively. The effects of the traveling-wave electrode structure and the phase-reversal process are represented in the term $A(\omega)$, which was derived in [9] from Alferness's equations [8]

$$A(\omega) = -\frac{\pi n_o^3 r_{ij} \Gamma_{eo}}{2G_e \lambda} \frac{1}{Z_M(\omega, L_e)} \times \left\{ \sum_{m=0}^{\infty} (-1)^m \int_{z_m}^{z_{m+1}} Z_M(\omega, z) \cos(\beta_e \delta z) dz \right\}. \quad (6)$$

In this equation, n_o is the optical refractive index of the modulator electrodes, r_{ij} is the electro-optic tensor in the external modulator material (with units of $\text{m}\cdot\text{V}^{-1}$), G_e is the inter-electrode gap, Γ_{eo} is the overlap integral between the applied electric field and the optical mode, and λ is the optical wavelength. The "walk-off" coefficient δ is defined as follows:

$$\delta \equiv 1 - \frac{n_o}{\sqrt{\epsilon_{\text{eff}}}} \quad (7)$$

where the effective dielectric constant of the transmission line ϵ_{eff} is calculated from known and measurable characteristics of the modulator electrodes. The terms n_o and r_{ij} are also known for any modulator substrate, G_e , z_m , and Z_t are easily measured, and Z_C , α_e , and β_e are determined from the modulator's equivalent circuit model.

B. Detector

The detector in the optical receiver module [Fig. 1(c)] is a reverse-biased photodiode with resistance R_j and capacitance C_j . It is coupled to the output circuit with parasitic resistance R_D and inductance L_D . In our model, we assume that the detector dc bias voltage is sufficiently large to ensure that it doesn't impose an upper limit on the link's RF power handling capability.

The ratio of detector photocurrent I_D to P_{opt} is $L_F K_{\text{FD}} \eta_D |H_D|$, where L_F is the attenuation loss in the fiber and at any fiber connectors, K_{FD} is the fiber-to-detector coupling efficiency, η_D is the detector responsivity, and $|H_D|$ is the detector frequency response, given by

$$|H_D|^2 = \frac{1}{1 + \left[\frac{\omega}{2\pi f_{3 \text{ dB}}} \right]^2} \quad (8)$$

where the bias-dependent term $f_{3 \text{ dB}}$ is the frequency at which the detector's responsivity to incident RF-modulated optical power falls off by 3 dB relative to the dc responsivity η_D .

C. Gain Analysis

The small-signal gain of an external modulation link employing a lumped-element modulator was derived using the signal flow diagram (SFD) technique in [6]. The majority of that analysis holds for the traveling-wave modulator case as well. All changes to the model in [6] resulting from the use of a traveling-wave modulator are embodied in (1)–(8).

As was shown in [6], small-signal approximations of the Bessel functions are used to calculate the link gain. For small v_M (compared to V_π), (4) above reduces to

$$P_{\text{opt}}(\omega) = \frac{A(\omega_1)}{\pi} v_M L_M P_L \cos\left(\frac{\pi V_b}{V_\pi}\right) \quad (9)$$

which is analogous to an expression in [6] which was applied in the lumped-element modulator case (and as such did not account for the effects in the $A(\omega)$ term). Expressions derived in this paper for a traveling-wave modulator yield the following revised equation for the small-signal gain of a traveling-wave modulator-based external modulation link

$$G = \left(\frac{A(\omega) L_M L_F K_{\text{FD}} \eta_D P_L |H_D| Z_0}{\pi} \right)^2 \times \frac{|S_{21M}|^2 |S_{21D}|^2 |1 + \Gamma_M|^2}{|1 - S_{22M} \Gamma_M|^2 |1 - S_{11D} \Gamma_{SD}|^2} \cos^2\left(\frac{\pi V_b}{V_\pi}\right). \quad (10)$$

D. Noise Analysis

Analytical determination of the link noise figure (NF) requires calculation of $N_{\text{out},RX}$, the noise power at the output of the link at the modulation frequency. $N_{\text{out},RX}$ is the total of: 1) $N_{\text{th},TX}$, the optical transmitter's thermal noise; 2) $N_{\text{th},RX}$, the optical receiver's thermal noise; and 3) N_{op} , the noise arising from optical generation and detection of the signal, i.e.,

$$N_{\text{out},RX} = N_{\text{th},TX} + N_{\text{th},RX} + N_{\text{op}} \quad (11)$$

where it has already been shown [6] that

$$N_{\text{th},TX} = \left| \frac{\sqrt{\langle v_{\text{th},TX}^2 \rangle B} Z_{\text{th},M}}{Z_{\text{th},M} + Z_0} \right|^2 \cdot \frac{G}{Z_0} = \frac{4k_B T B |Z_{\text{th},M}|^2 (Z_0 + \text{Re}Z_{\text{th},M})}{|Z_{\text{th},M} + Z_0|^2 Z_0} G \quad (12)$$

$$N_{\text{th},RX} = \left| \frac{\sqrt{\langle v_{\text{th},RX}^2 \rangle B} Z_0}{Z_{\text{th},D} + Z_0} \right|^2 \cdot \frac{1}{Z_0} = \frac{4k_B T B \cdot \text{Re}Z_{\text{th},D} \cdot Z_0}{|Z_{\text{th},D} + Z_0|^2} \quad (13)$$

and

$$N_{\text{op}} = \left\{ [L_F K_{\text{FD}} \eta_D P_{\text{out}}(\text{DC})]^2 \text{RIN}(\omega) + 2e L_F K_{\text{FD}} \eta_D \times P_{\text{opt}}(\text{DC}) \right\} \frac{|S_{21D}|^2}{|1 - S_{11D} \Gamma_{SD}|^2} B Z_0. \quad (14)$$

In these equations, Z_0 is the impedance of the input and output of the link, $\text{RIN}(\omega)$ is the laser's relative intensity noise (RIN), e is the electronic charge, and the detector's dark current is assumed to be negligible. All other terms are defined previously or in Fig. 1. Using (11)–(14) to determine $N_{\text{out},RX}$, the NF of the link is calculated as follows [6]:

$$\text{NF} = \frac{N_{\text{out},RX}}{k_B T B G}, \quad (15)$$

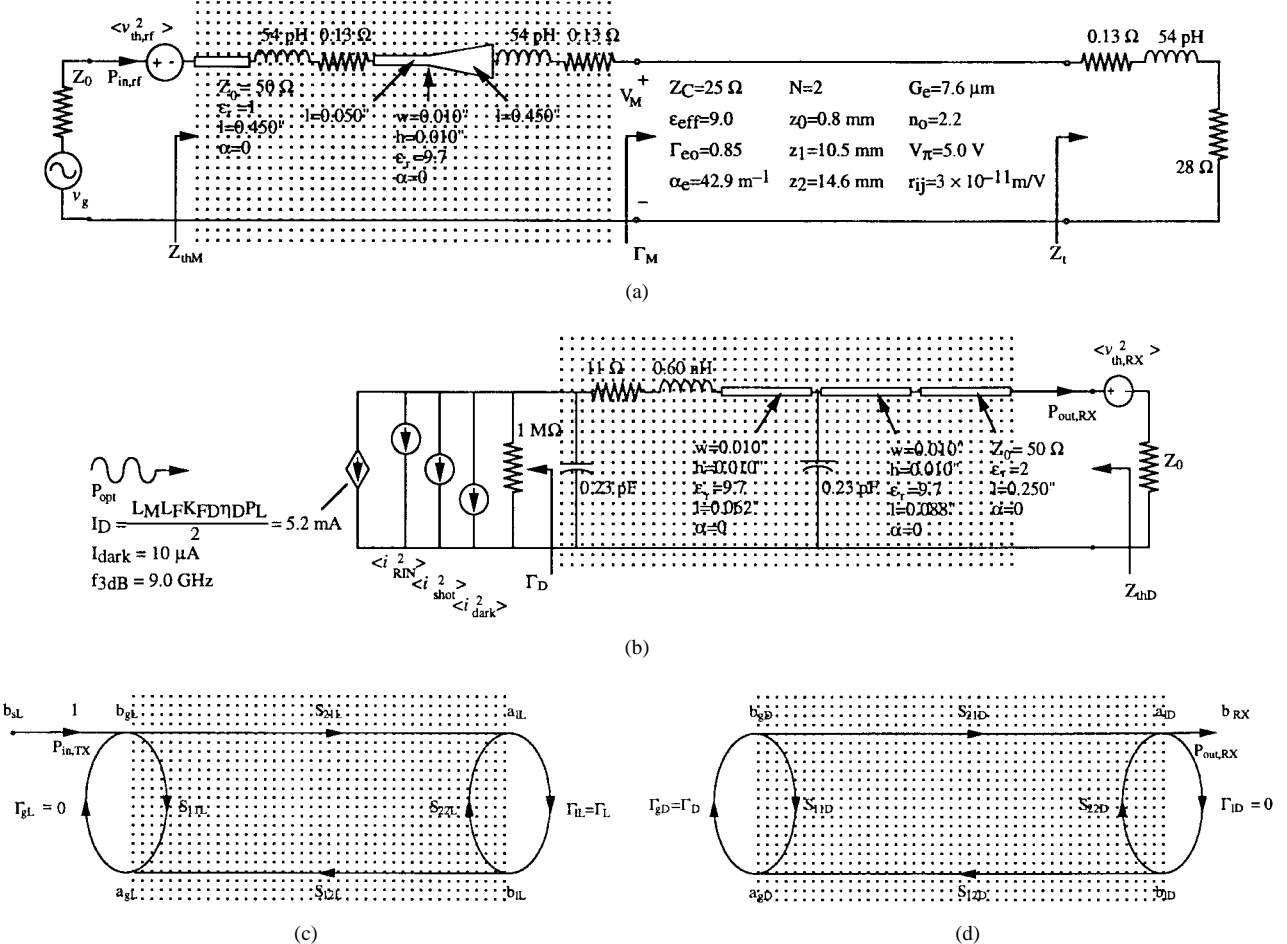


Fig. 2. Equivalent circuit model of external modulation link optimized across a wide microwave bandwidth (6–12 GHz). (a) Equivalent circuit of electro-optic modulator-based optical transmitter. (b) Equivalent circuit of p-i-n photodiode-based optical receiver. (c) SFD of electro-optic modulator-based optical transmitter. (d) SFD of p-i-n photodiode-based optical receiver.

E. Intermodulation Distortion Analysis

The upper limit to spurious-free DR (SFDR) of an external modulation fiber-optic link is the third-order intercept input power $P_{in,int}$, for which the output powers at the fundamental and third-order intermodulation frequencies are equal. $P_{in,int}$ was derived in [6] for the lumped-element electrode case. The only difference which must be taken into account when a traveling-wave modulator is used instead is the modified argument of the Bessel functions, resulting in

$$P_{in,int} = \frac{\pi^2 |1 - S_{22M} \Gamma_M|^2}{2[A(\omega)]^2 |S_{21M}|^2 |1 + \Gamma_M|^2 Z_0}. \quad (16)$$

This parameter and the NF together set the SFDR [6] as follows:

$$\text{SFDR} = \left(\frac{P_{in,int}}{k_B T B N F} \right)^{\frac{2}{3}}. \quad (17)$$

III. EXPERIMENTAL VERIFICATION OF THE MODEL

To assess the validity of the model, we compare its predictions to the measured performance of an experimental external modulation link. This section describes a link using a traveling-wave modulator designed for operation across

a broad microwave frequency band (6–12 GHz). All link measurements were performed at the modulator's quarter-wave voltage ($V_b = 0$), the modulator's bias-dependent behavior modeling having been established in [7].

A. Device Selection and Modeling

An LiNbO₃ Mach-Zehnder device manufactured by uniphase telecommunications products (UTP's) is selected as the external modulator. This modulator has achieved a bandpass response between approximately 1–19 GHz by using a two-section phase-reversal traveling-wave electrode structure, and exhibits a 29-dB extinction ratio when TE-polarized light at $\lambda = 1.3 \mu\text{m}$ is launched into its polarization-preserving input single-mode fiber pigtail. Its dc half-wave voltage V_π is measured as 4.4 V. For the detector an InGaAs p-i-n photodiode is selected with a dc responsivity of $\eta_D = 0.80 \text{ A/W}$ and a measured 3-dB modulation bandwidth, f_{3dB} , of 9 GHz when reverse-biased at 20 V. The photodetector is mounted in a standard microwave test fixture to enable de-embedding its impedance out of the measured scattering parameter of the device in the test fixture [6].

TABLE I
SUMMARY OF THE BROAD-BAND MICROWAVE EXTERNAL MODULATION LINK PERFORMANCE AT 6, 9, AND 12 GHz.
MEASURED AND MODELED RESULTS ARE GIVEN

Frequency (GHz)		6.0	9.0	12.0
Gain (dB)	Model	-31.8	-30.7	-36.2
	Measurement	-31.0	-31.3	-35.5
Noise Figure (dB)	Model	44.8	45.7	48.0
	Measurement	46.0	47.5	50.0
Spurious-Free Dynamic Range (dB in 1 MHz)	Model	65.4	64.8	63.4
	Measurement	66.7	66.9	65.5

Equivalent circuit models of the electro-optic modulator and detector are obtained by using SuperCompact¹ to fit values of L_{PM} , R_{PM} , and Z_t for the modulator [cf. Fig. 1(b)] and C_j , R_j , R_D , and L_D for the detector [cf. Fig. 1(c)] to the de-embedded impedances of these devices. The equivalent circuit models have made it possible to determine how the $50\text{-}\Omega$ input and output microstrip transmission lines in the modulator and detector packages, respectively, could be altered to yield a link insertion loss characteristic which is as flat as possible across the link-design frequency band of 6.0–12.0 GHz. Fig. 2 depicts the equivalent circuit models of the reactive impedance-matching circuits optimized in this way. Return losses of 13.5 and 6.3 dB are measured at 12 GHz for the traveling-wave modulator and detector, respectively, when the circuit component values are adjusted to achieve optimum gain flatness.

In order to maximize the performance of the external modulation link, a single-mode fiber-pigtailed Nd:YAG laser with 40 mW of optical power at $\lambda = 1.3 \mu\text{m}$ is used as the optical source. The laser and the optical receiver are optically coupled to the modulator's input and output fibers, respectively, and the input optical polarization is adjusted to maximize the ratio of optical power measured at the “on” and “off” modulator voltages. At the quarter-wave bias point ($V_b = 0$), a dc photocurrent of 5.2 mA is measured.

The frequency-dependent parameter $\text{RIN}(\omega)$ is calculated from an optical noise power measurement using an RF spectrum analyzer with an optical input port. The equivalent circuit models of the optical transmitter and receiver modules are used to determine values for all the other frequency-dependent parameters—namely Z_C , Z_t , $[S_{ijM}]$, Z_{thM} , $[S_{ijD}]$, and Z_{thD} —at frequencies between 5–15 GHz. These parameters, along with those indicated in Fig. 2, are used in (1)–(17) to predict G , NF, and SFDR for the experimental link.

B. Link Measurements

Table I summarizes the measured performance of the experimental external modulation link at three frequencies—6, 9, and 12 GHz—and compares it to the performance predicted by the model at these frequencies. For the quarter-wave bias voltage ($V_b = 0$), the insertion gain predicted by the model is plotted in Fig. 3 alongside the insertion gain of the link as measured using an RF network analyzer. Both curves exhibit

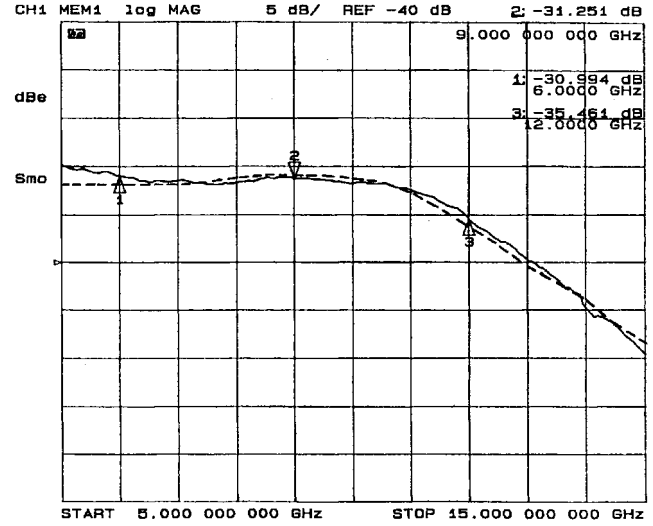


Fig. 3. Insertion loss of the experimental external modulation fiber-optic link when the modulator is biased at the quarter-wave voltage $V_b = 0$. The measured result is shown along with the performance predicted using the model.

3-dB rolloff frequencies at about 12 GHz, and peak at roughly 9 GHz. The curve shapes also track fairly well, showing that the model serves to adequately predict the performance of a broad-band microwave link.

Using (11)–(15), the link's noise is calculated at 6, 9, and 12 GHz. The NF was also experimentally determined using an RF noise measurement setup described in [6]. As listed in Table I, the NF measured at 9 GHz is 47.5 dB. This nearly matches the analytically determined 9-GHz NF result of 45.7 dB.

The two-tone intermodulation distortion of the link is measured at two third-order intermodulation product frequencies surrounding microwave carrier frequencies of 6, 9, and 12 GHz using an experimental setup described in [7]. Table I lists the SFDR determined from these measurements, as well as the DR predicted by the link model. The tendency for the model to be somewhat pessimistic in its SFDR predictions, as shown in Table I, could be due to the difficulty with which electrical parasitic parameters are pinpointed in the optical transmitter and receiver equivalent circuit models. In fact, at the microwave frequencies above 6 GHz, inductance errors of less than 0.1 nH and line-length errors of less than 0.1 mm are sufficient to cause significant discrepancies between a physical device's or circuit's behavior and that of its equivalent circuit model.

¹SuperCompact is a trademark of Compact Software, Inc., Paterson, NJ.

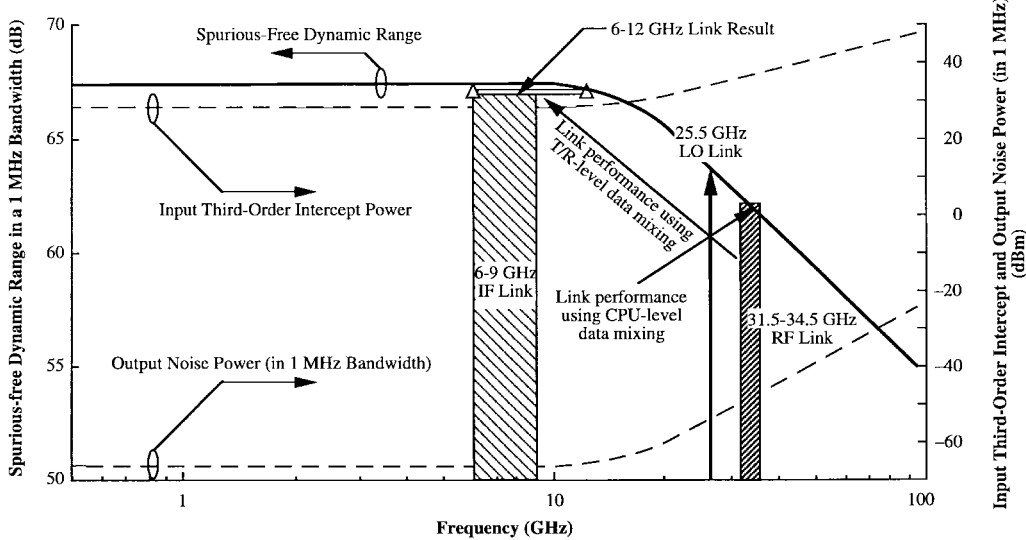


Fig. 4. Example of how using the T/R-level data-mixing architecture enables millimeter-wave link performance which can only be achieved at much lower microwave frequencies if the conventional CPU-level data-mixing architecture is used.

IV. TRANSMIT/RECEIVE MODULE-LEVEL DATA-MIXING ARCHITECTURE

Most antenna-remoting system architectures use mixers to down-convert RF signals to IF frequencies at the output of the coax-cable or fiber-optic remoting links (i.e., at the central processing unit (CPU) level). Down-conversion can also be performed at the transmit/receive (T/R) module level [10]. Detailed block diagrams of the CPU-level and T/R-level data-mixing architectures have been presented elsewhere [11]. In the more conventional CPU-level data-mixing architecture, the single-sideband (SSB) mixing of an IF or baseband signal (with frequency f_{IF}) with a local oscillator (LO) (at frequency f_{LO}) generates the transmit RF signal ($f_{LO} + f_{IF}$). The same LO at the CPU can be used to down-convert the received RF signal. In the T/R-level data-mixing architecture, the high-frequency LO and IF data signals are separately imposed on two optical carriers, and are mixed at the antenna end of the link to construct or de-construct the desired RF signal. Thus, the performance of the LO link need only be optimized at a single high frequency (f_{LO}), and the IF data can be relayed efficiently and with low noise by a lower frequency microwave fiber-optic link. This usually results in improved RF performance, especially in cases where the desired RF frequency band is exceedingly high, broad, or both.

Fig. 4 renders as a function of frequency the input third-order intercept power, output noise power, and SFDR—calculated using our analytical model—which can be achieved using the components of our 6–12-GHz experimental link in the conventional CPU-level data-mixing configuration. The measured DR of the 6–12 GHz link is also shown.

Following through an example of a link using T/R-level data mixing illustrates the advantages of this architecture. As an example of SATCOM applications, a 31.5–34.5-GHz link is considered. Fig. 4 illustrates the extent to which performance is sacrificed at these frequencies when the CPU-level mixing approach is used, due to the fact that this architecture requires

the external modulator to function at RF frequencies beyond the walk-off frequencies of most currently available devices (arising from the microwave optical-wave velocity mismatch) and also demands a high-bandwidth detector with large power-handling capability.

The T/R-level data-mixing approach imparts design flexibility in that the 3-GHz RF bandwidth around a center frequency of 33 GHz can be achieved using any combination of narrow-band LO and broad-band IF fiber-optic links whose frequencies add up to 31.5–34.5 GHz. Fig. 4 shows the 6–12-GHz link described above being used from 6 to 9 GHz as the IF link in conjunction with a narrow-band 25.5-GHz LO link. RF-IF mixer technology is likely to reach the point where it can be assumed that the range of the resulting RF output powers from the mixed outputs of the IF and LO links will be essentially that of the IF link. Thus, T/R-level data mixing could result in 31.5–34.5-GHz link performance approximately equal to that of a 6–9-GHz link.

V. DISCUSSION AND CONCLUSIONS

For antenna-remoting applications at millimeter-wave frequencies above the rated bandwidths of commercially available electro-optic devices, it is expected that higher performance will be obtained using the T/R-level data-mixing architecture. Compared to the CPU-level data-mixing architecture, T/R-level data mixing requires that a mixer be located at the antenna along with a LO (unless the LO is delivered by a separate fiber-optic link). The payoff, however, lies in the fact that by using the nonlinearities of the modulator, detector, or mixer, much higher modulation frequencies can be obtained. For instance, at the antenna site, a millimeter-wave transmit RF signal can be constructed by mixing the optically fed IF signal with an n th-order harmonic of the optically fed microwave LO (using the mixer's nonlinearity to both up-convert and mix). In this way, the IF link can be operated at modest microwave frequencies where the electro-optic devices exhibit efficient and low-noise performance characteristics.

In conclusion, we have expanded previously published external modulation fiber-optic link performance models [6], [7] to predict the broad-band performance resulting from the use of a modulator with traveling-wave electrodes. We demonstrated the usefulness of the model by showing that it predicted fairly closely the measured gain, NF, and SFDR of a 6–12-GHz link which employed a LiNbO₃ traveling-wave external modulator. Finally, we used the model to compare the fiber-optic link performance enabled by two architectures—CPU-level data mixing and T/R-level data mixing. Assuming that we were not limited by the mixer's performance, we analytically showed that the T/R-level data-mixing architecture would enable millimeter-wave link performance which can only be achieved at much lower microwave frequencies if the CPU-level data-mixing architecture is used.

ACKNOWLEDGMENT

The authors thank M. McCabe-Bunya of Martin Marietta Corporation, Syracuse, NY, for assisting with the assembly of the detector module.

REFERENCES

- [1] B. Kolner and D. Bloom, "Electrooptic sampling in GaAs integrated circuits," *IEEE J. Quantum Electron.*, vol. QE-22, pp. 79–93, Jan. 1986.
- [2] W. Stephens and T. Joseph, "System characteristics of direct modulated and externally modulated RF fiber-optic links," *J. Lightwave Technol.*, vol. LT-5, pp. 380–387, Mar. 1987.
- [3] C. Bulmer and W. Burns, "Linear interferometric modulators in Ti:LiNbO₃," *J. Lightwave Technol.*, vol. LT-2, pp. 512–521, Aug. 1984.
- [4] B. Kolner and D. Dolfi, "Intermodulation distortion and compression in an integrated electrooptic modulator," *Appl. Opt.*, vol. 26, pp. 3676–3680, 1987.
- [5] C. Cox III, G. Betts, and L. Johnson, "An analytic and experimental comparison of direct and external modulation in analog fiber-optic links," *IEEE Trans. Microwave Theory Tech.*, vol. 38, pp. 501–509, May 1990.
- [6] A. Daryoush, E. Ackerman, N. Samant, S. Wanuga, and D. Kasemset, "Interfaces for high-speed fiber-optic links," *IEEE Trans. Microwave Theory Tech.*, vol. 39, pp. 2031–2044, Dec. 1991.
- [7] E. Ackerman, S. Wanuga, D. Kasemset, A. Daryoush, and N. Samant, "Maximum dynamic range operation of a microwave external modulation link," *IEEE Trans. Microwave Theory Tech.*, vol. 41, pp. 1299–1306, Aug. 1993.
- [8] R. Alferness, "Waveguide electrooptic modulators," *IEEE Trans. Microwave Theory Tech.*, vol. MTT-30, pp. 1121–1137, Aug. 1982.
- [9] E. Ackerman, "System-level performance evaluation of microwave fiber-optic links," Ph.D. dissertation, Dept. Elect. Comput. Eng., Drexel Univ., Philadelphia, PA, 1994.
- [10] K. Williams and R. Esman, "Optically amplified downconverting link with shot-noise-limited performance," *IEEE Photon. Technol. Lett.*, vol. 8, pp. 148–150, Jan. 1996.
- [11] R. Saedi, W. Jen, N. Samant, A. Daryoush, D. Sturzebecher, and P. Herczfeld, "Comparison of CPU level data mixing to T/R level data mixing architectures in optically controlled phased arrays," in *IEEE Microwave Theory Tech. Symp. Dig.*, Atlanta, GA, May 1993, pp. 501–504.

Edward I. Ackerman (S'86–M'87), for a photograph and biography, see this issue, p. 1383.

Afshin S. Daryoush (S'84–M'86–SM'91), for a photograph and biography, see this issue, p. 1295.